Korean J. Chem. Eng., 39(8), 2239-2251 (2022)
DOI: 10.1007/s11814-022-1119-y

pISSN: 0256-1115
eISSN: 1975-7220

Electroactive adsorbent composites of porous graphite carbon/carbon nanotube for highly efficient organic dye removal

Sabrine Zghal*, Ilyes Jedidi,†, Marc Cretin***,†, Sophie Cerneaux***, Didier Cot***, Serge Lagerge***, Stefano Deabate***, and Makki Abdelmouleh*,†**

*Laboratory of Materials Science and Environment (LMSE), Faculty of Science of Sfax (University of Sfax), Rte. Soukra Km 4, 3000 Sfax, Tunisia
**University of Technology and Applied Science - Sohar, Engineering Department, Al-Jamiaa street, P.O. Box, 135, Sohar, 311, OMAN
***Institut Européen des Membranes, IEM - UMR 5635, ENSCM, CNRS, Univ Montpellier, Montpellier, France
(*Received 6 November 2021 • Revised 2 March 2022 • Accepted 17 March 2022*)

Abstract−The highest total organic carbon (TOC) and color removal efficiency of Acid Orange 7 (0.1 mM initial concentration) on graphite carbon/carbon nanotubes electrodes (KS44/CNT) reached more than 98% in three hours of Electro-Fenton (EF) treatment under optimal conditions (pH=3 and I=20 mA), compared to carbon graphite electrode developed without carbon nanotubes (KS44-0). The apparent kinetic constants of degradation were 0.17 and 0.12 min^{-1} for the KS44-(20)/CNT and KS44-0, respectively. The long-term stability and system durability were attributed to the graphite carbon/CNT electrodes due to continuous operating treatment that allowed processing efficiency and reusability without any decrease of the catalytic activity in time after five cycles of use. Regardless of the medium, superior decolorization and TOC removal efficiency were obtained for electrodes (KS44-(20)/CNT) containing 20 wt% of ferrocene powder as catalyst for CNTs' growth and iron nanoparticle establishment. Furthermore, the presence of CNTs and iron particles as precursors enhanced drastically the electrochemical and physical properties of the electrode synthesized in a one-step process. The results confirmed that carbon electrodes behave as multifunctional materials acting both as adsorbent and active cathode in the electro-Fenton process for the destruction and total mineralization of Acid Orange 7 (AO7) as a model for organic contaminated wastewater.

Keywords: Carbon Nanotubes, Acid Orange 7, Adsorption, Electro-Fenton, Degradation-mineralization

INTRODUCTION

The widespread contamination of soil and groundwater by synthetic organic chemicals (e.g., dyes) has been recognized as an issue of growing importance in recent years. Such substances with considerable coloring capacity are widely employed in the textile, pharmaceutical, food, cosmetics, plastics, photographic and paper industries [1,2]. To solve the problems of toxicity, mutagenicity and carcinogenicity of dye products, advanced oxidation processes (AOPs) are frequently used. The particularity of these processes arises from the generation of radicals in the aqueous medium that are highly reactive towards the oxidation of molecular entities.

The combination of H_2O_2 and Fe^{2+}, called Fenton reagent, is an effective route for the mediated mineralization of a wide variety of organic substrates [3-5] thanks to the production of hydroxyl radical ($^{\bullet}OH$) as indicated in Eq. (1):

$$H_2O_2+Fe^{2+}\rightarrow OH^-+Fe^{3+}+{}^{\bullet}OH \quad (1)$$

In the Fenton process, the pH of the aqueous solution must be maintained at a value close to 3 to avoid the precipitation of iron III [3] (Eq. (2)):

$$H_2O_2+Fe^{2+}+H^+\rightarrow H_2O+Fe^{3+}+{}^{\bullet}OH \quad (2)$$

Fenton reagents can be produced electrochemically in solution. Hence, the continuous electrogeneration of hydrogen peroxide (H_2O_2) in an acidic solution is conducted by a two-electron reduction of molecular oxygen, expressed as follows in Eq. (3):

$$O_2+2H^++2e^-\rightarrow H_2O_2 \quad (3)$$

Moreover, the propagation of the Fenton reaction is based on the regeneration of the ferrous ions (initially introduced) by direct reduction (Eq. (4)) at the cathode of Fe^{3+} formed in Eq. (2).

$$Fe^{3+}+e^-\rightarrow Fe^{2+} \quad (4)$$

The process combining the electrochemical generation of H_2O_2 from O_2 reduction and the regeneration of Fe^{2+} from Fe^{3+} to get continuously, Eq. (2) is called the electro-Fenton (EF) process [6] and is more and more developed for the treatment of contaminated water especially for biorefractory pollutants [6-9].

In previous research works, chemically modified carbon felt (CF) electrodes were used for electro-Fenton process in order to eliminate biorefractory compounds from aqueous medium. Graphene oxide modified CF was observed to increase the mineralization rate

†To whom correspondence should be addressed.
E-mail: ilyesjedidi.soh@cas.edu.om, marc.cretin@umontpellier.fr, makki.abdmouleh@fss.rnu.tn

of the azo dye AO7 [10]. CF decorated with nanoparticles of Fe^{II}/Fe^{III} layered double hydroxides (LDH) has proven its efficiency towards the heterogeneous EF process for sulfamethoxazole mineralization over a wide pH range [11]. Furthermore, nitrogen-doped graphitized CF cathode [12] as well as carbon nanotube fiber-based materials [13] were successfully developed as cathodes for coupling a pre-adsorption step of pollutant before their *in situ* mineralization by EF process. In virtually all these studies, focusing on the use of commercial carbon felts as cathodes for the preparation of high-performance electrode materials for the electro-Fenton (EF) process, the experimental results lead to the almost complete mineralization of organic azo dyes. According to Le et al., the results demonstrated that graphene-based cathodes could be used for the degradation and mineralization of azo dyes, taking into account their innovative role in the electro-Fenton reaction as promising reverie for applications in wastewater treatment [11,14].

Recently, porous graphite carbon/carbon nanotubes composite was prepared in a one-step process by carbonization under an inert atmosphere at 800 °C [15]. Carbon nanotubes (CNTs) were grown *in situ* simultaneously with the formation of the porous graphite carbon/CNT composite using ferrocene as catalyst for CNTs growth, phenolic resin and graphite powder as precursors [15]. Thanks to their effective surface properties, significant electrical conductivity, chemical resistance and thermal stability, excellent behavior was enhanced by the presence of CNTs when tested as adsorbent for humic acid and copper (II) ions from aqueous solutions [15]. The main objective of the present research work (Schema 1) is to investigate the electrochemical performance of the as-prepared porous graphite carbon/carbon nanotubes composites as a novel multifunctional material acting as both adsorbent and active cathode in the electro-Fenton process (EF). The use of EF process is to remove and destroy toxic and non-biodegradable organic pollutants and to solve their harmful effects and problems of toxicity, mutagenicity and carcinogenicity to human health and aquatic life [16-19]. Long-term stability testing was carried out to provide evidence of system durability and reusability without any decrease of the catalytic activity in time and desorption conditions [20-22].

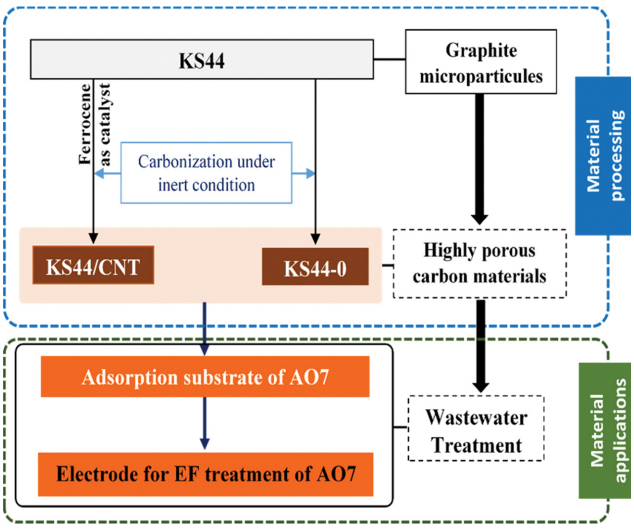

Schema 1. Schematic representation of the work objective.

Azo dyes are most commonly used due to the presence of the azo group (-N=N-), giving these chemicals some resistance to light, acids, bases and oxygen, which are desired properties for clothing [23]. Note that more than 60% of the world production of dye is used by the textile industries and more than one half of this quantity is discharged into the receiving water more or less without treatment [24]. More than 53% of the azo dyes used are identified as being stable and non-biodegradable compounds [24]. Acid Orange 7 (AO7) was used here as a model of azo dye molecule that is persistent in the environment and was tested to prove the efficiency of materials towards its degradation and total mineralization.

EXPERIMENTAL

1. Materials

Pure graphite powder designated as KS44 with a mean particle size of 44 μm used as carbon source was kindly provided by TIMCAL Group (Switzerland). Organic additives such as Avicel® and ethylene glycol were purchased from Sigma-Aldrich. Novolac® type phenolic resin acting as binder was kindly supplied by Sumitomo Bakelite Europe (Barcelona). Ferrocene powder $Fe(C_5H_5)_2$ from Sigma-Aldrich was used as catalyst for CNTs growth.

AO7 (Acid Orange 7), 4-(2-Hydroxy-1-naphthylazo) benzenesulfonic acid sodium salt, anhydrous sodium sulfate (Na_2SO_4, 99.0-100.5%), iron (II) sulfate heptahydrate ($FeSO_4{\cdot}7H_2O$, (>99% purity)) and sulfuric acid (95-97%) were purchased from Sigma-Aldrich. Total organic carbon (TOC) standard of 1000, mg/L (Sigma-Aldrich) and sodium hydrogen carbonate (99.5%, ACS, Karlsruhe) were used for calibration.

2. Synthesis of Highly Porous Carbon Materials

The paste formulation of porous carbon composites (see Table S1) was chosen based on our previous study about porous carbon composite preparation [15]. The solutions obtained after dissolving the powdered phenolic resin (Novolac®) in ethanol were added in separate doses to the dry mixture of graphite powder, organic additives and ferrocene powder. The found pastes were subjected to a thermal treatment in a tubular electrical furnace (VTF7 VECSTAR) at 150 °C for 12 h in the presence of air for a total cure. Next, solidified tubes were carbonized under a nitrogen flow, raising the temperature to 800 °C with a speed of 2 °C·min^{-1}, followed by a 1 h dwelling step at 800 °C and then a free cooling step down to room temperature to yield the final electrode material. In the present research work, five types of electrode were developed, namely KS44-0, KS44-(15)/CNT, KS44-(20)/CNT and KS44-(25)/CNT electrodes, containing an initial weight ratio of ferrocene of 0, 15, 20 and 25%, respectively.

3. Removal of Acid Orange 7 by Adsorption and Electro-Fenton Process

The adsorption experiments were performed in bakers in which 0,4 g (W) of electrode composites (20 mm length×10 mm width×3 mm thickness) was contacted with 10 mL (V) of AO7 aqueous solutions at various initial concentrations (C_0) ranging from 0.01 to 1 mM. The systems were equilibrated (by gentle agitation for 2 hours) at a constant temperature in a thermostat at 298 K±1. Subsequently, the solute (AO7) equilibrium concentrations in the equilibrated supernatant phases, C_e, were measured using a Spectropho-

tometer Jenway 6300 (Barioworld Scientific Ltd., Dunmow, U.K.) at the maximal absorbance wavelength of 484 nm. The amount of adsorption was calculated according to the following equation [25]:

$$q_e = \frac{(C_0 - C_e)V}{W} \quad (5)$$

where q_e is the amount of AO7 adsorbed onto the unit amount of graphite electrodes ($mg \cdot g^{-1}$), C_0 and C_e are the initial and equilibrium concentrations of AO7 ($mg \cdot L^{-1}$), respectively. V is the volume of AO7 solution (L) and W is the weight of graphite electrode (g).

Electro-Fenton experiments were performed at room temperature in a 20 mL undivided cylindrical glass cell equipped with two electrodes. The as-prepared carbon material of 2 cm^2 area was used as working electrode functions as a cathode and a platinum (2 cm× 5 cm) sheet as auxiliary electrode functions as an anode. The distance between the working and auxiliary electrodes was 2 cm. As for the applied current, it was controlled using a power supply (Lambda Electronic, USA) in a galvanostatic mode.

For the electrochemical degradation, an AO7 solution was used as model pollutant whose initial concentration was fixed at 0.1 mM. A 50 mM Na_2SO_4 solution was added, under magnetic stirring (900 rpm) at room temperature, to an AO7 solution as supporting electrolyte and $FeSO_4 \cdot 7H_2O$ (0.2 mM) as catalyst. The whole solution was acidified with a 1 M sulfuric acid (H_2SO_4) solution to adjust the pH when necessary.

The synthesized materials were immersed in 10 mL of the above stirred final solution. Air was bubbled for 5 min to saturate the aqueous solution, then the electric power was turned on at 20 mA and the electro-Fenton reaction started simultaneously (Schema 2).

The efficiency of the electro-Fenton process was followed by monitoring the absorbance of the solution at λ=484 nm.

4. Characterization

The porosity and the average pore diameter of the final carbonized materials were determined by mercury intrusion porosimetry using an Autopore IV 9500 V1.06 apparatus (Micromeritics Instrument Corporation). The specific surface area of the synthesized samples was determined by volumetric adsorption/desorption measurement at 77 K of nitrogen using the Micromeritics ASAP 2020 Surface Area and Porosity analyzer, by applying the B.E.T method with molecular cross-section surface area being 16.2 $Å^2$ for nitrogen. Further morphological and structural characterizations were performed by Field-emission scanning electron microscopy (FE-SEM) (ZEISS Gemini SEM 500 microscope). Contact angle measurements were carried out by depositing calibrated liquid drops of water on the porous carbon materials. The measurement of the angle was from images captured by a camera monitored by a computer. The WINGOUTTE software allowed determining the contact angle by the interpolation arcs methods of the drop contour. Raman spectroscopy measurements were carried out under ambient conditions using an argon-ion laser (Perx 1877 triple meet Spectrometer, USA) tuned to 659.55 nm and a laser power of 150 mW. Electrical conductivity measurements were carried out on flat supports using a four-point probe (points located at the corners of a square of 1 cm side). The equipment used was the HL 5500 Hall system from Nanometrics Company. The measured resistance corresponded to an average of three measurements performed in various areas of the composite surface. The electrolysis process was carried out with a Hameg HM8040 triple power supply at constant current. The absorbance of AO7 was measured using a spectrophotometer, Jenway 6300 (Barioworld Scientific Ltd., Dunmow, U.K.). To determine the concentration of AO7, a calibration curve was established at the maximal absorbance wavelength of 484 nm. Total organic carbon (TOC) removal was measured with a TOC-L CSH/CSN Shimadzu (Japan) analyzer. Calibration curves for total carbon (TC) and inorganic carbon (IC) analysis were built up by automatic dilution of standard solutions of potassium hydrogenophtalate for TC and sodium hydrogen carbonate for IC.

RESULTS AND DISCUSSION

1. Characterizations of Composite Electrode Materials

Table 1 shows the porosity, the pore size, the specific surface area of the pure carbon graphite (KS44-0) and the different graphite carbon/CNT composites KS44-(15)/CNT, KS44-(20)/CNT and KS44-(25)/CNT. For all composites, we observed a high porosity that was mainly created by the different carbonaceous material

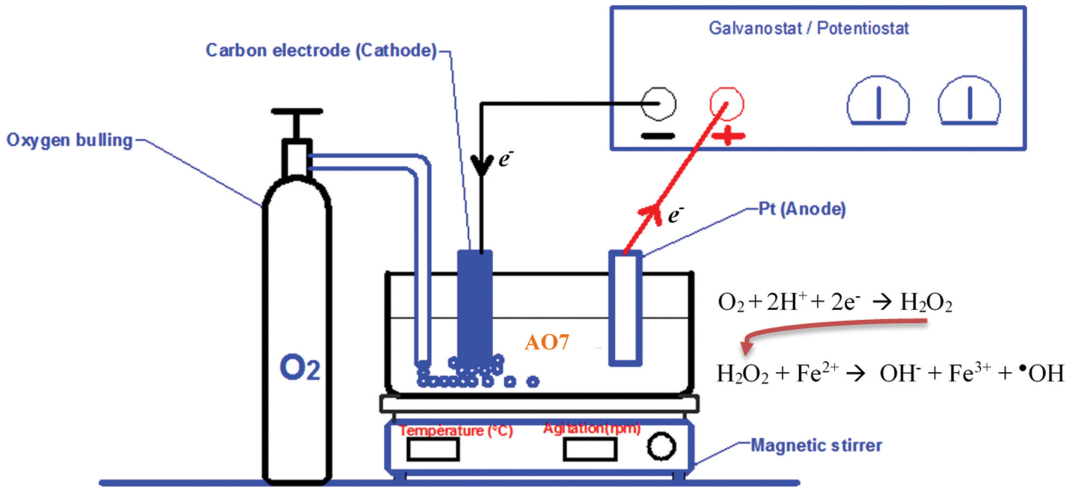

Schema 2. Electro-Fenton experimental setup for the degradation and mineralization of AO7.

Table 1. Porosity, specific surface area and average pore size of carbon composites

Composites	KS44-0	KS44-15/CNT	KS44-20/CNT	KS44-25/CNT
Porosity (%)	45.4	51.2	52.3	54.6
Specific surface area, As (m^2/g)	85.6	124.8	131.4	134
Average pore size (nm)	1.90	3.30	3.39	3.44

(organic additives and phenolic resin) decomposition in addition to ferrocene in the case of the graphite carbon/CNT specimens [15]. As measured by the BET method, the specific surface area increases from KS44-0 to KS44-25/CNT (Table 1). This significant increase is mainly due to the porosity which is linked to the presence of CNTs in the structure of the electrodes. Indeed, other than the porosity and pore size distribution of the composites, the specific surface area is influenced, but in a lesser extent, by area density, size, shape and surface roughness of carbon nanotube [26]. The evolution of the contact angle of a water drop deposited on the surface of the carbon graphite (KS44-0) and carbon graphite/NTC (KS44-15, KS44-20 and KS44-25) support samples is shown in Fig. 1. A value of around 43°, which remains stable for the duration of the measurement time is observed for (KS44-0). The low obtained value for (KS44-0) is mainly linked to the porous structure of the material obtained following the sublimation of the pore-forming additives and the loss in mass of the resin by carbonization step under nitrogen. However, an increase in the value of the contact angle is observed at 70, 88 and 81°, respectively, for the KS44-15, KS44-20 and KS44-25. Therefore, the growth of CNTs (whose ultra-hydrophobic character) in the pores and on the surface is the cause of the inaccessibility of water molecules in the pores of composites.

The nitrogen adsorption-desorption isotherms and the corresponding pore size distributions of the porous carbon composites are shown in Fig. S1. According to IUPAC classification of adsorp-

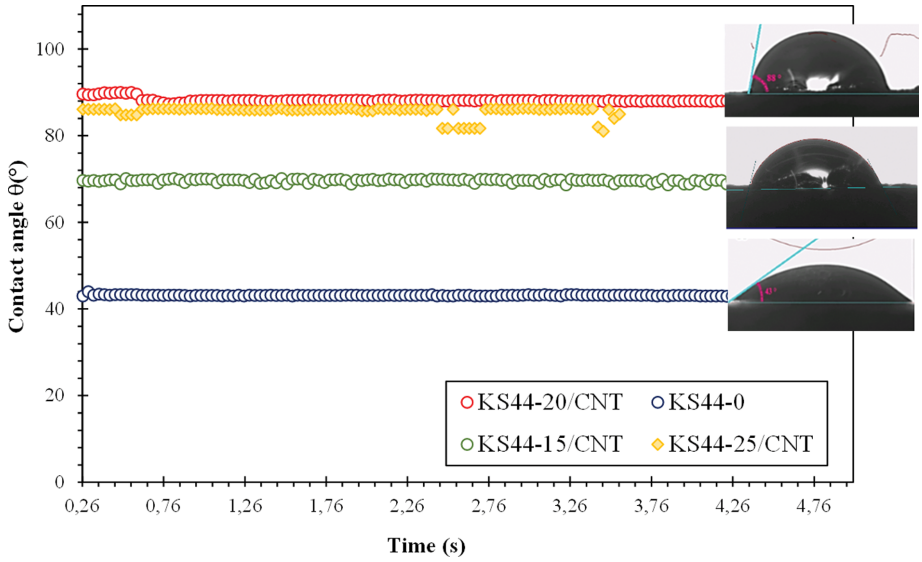

Fig. 1. Water contact angle evolution of porous carbon materials at different percentage of Ferrocene.

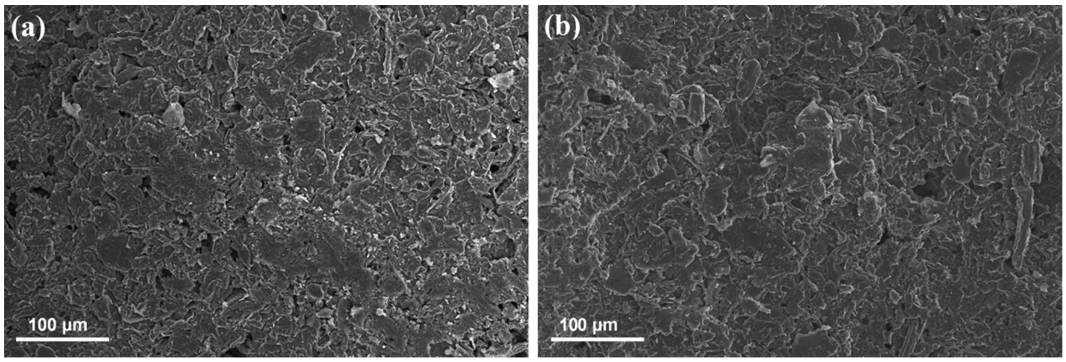

Fig. 2. SEM images of graphite carbon/CNT electrodes: (a) KS44-(20)/CNT, (b) KS44(15)/NTC.

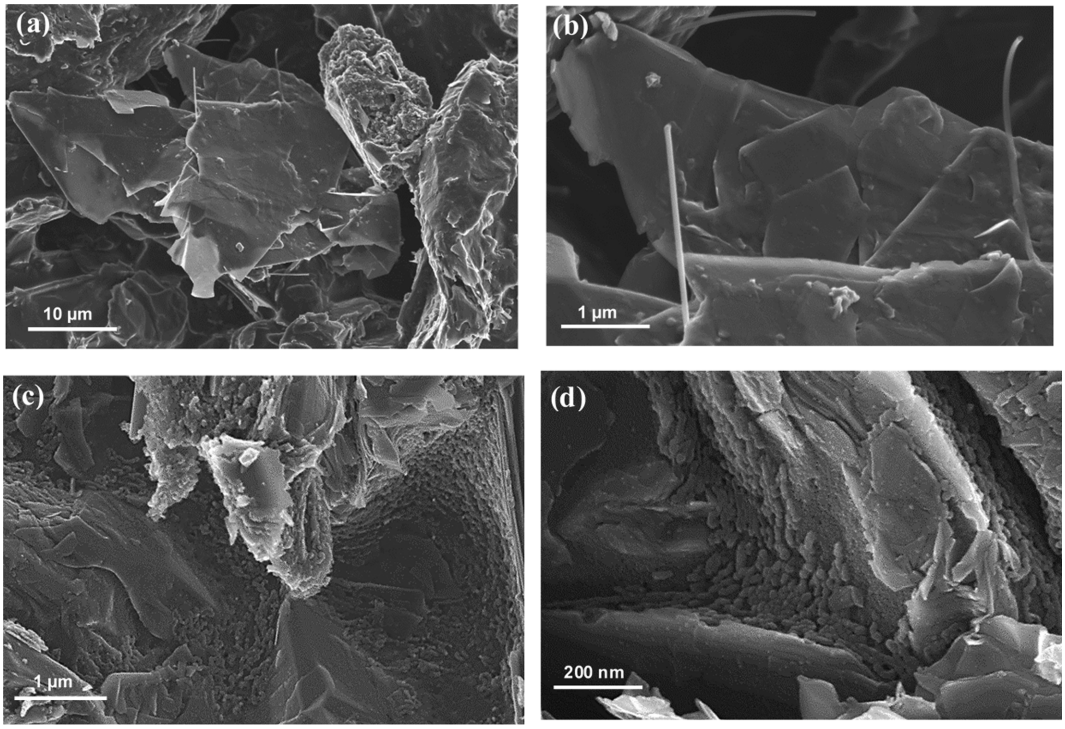

Fig. 3. SEM images at different scales of KS44-(20)/CNT.

tion isotherms [27], the graphite carbon composite (KS44-0) exhibited type-I isotherm, thus indicating the main mechanisms governing the absorption of gases by microporous adsorbents. The limiting uptake depends on the accessible micropores volume. On the opposite, the graphite carbon/carbon nanotubes composites (KS44/CNT) displayed a typical type-IV isotherm with a hysteresis loop. Furthermore, a clear step associated with the filling of accessible mesopores due to capillary condensation occurs at approximately P/P_0= 0.4-0.9. The summary of the average pore size for all the carbon composites is presented in Table 1.

The SEM micrographs presented in Fig. 2 underscore that the KS44-(20)/CNT composite presents more porous structure than that of KS44-(15)/CNT. This increase, which is correlated with the measurement of porosity, is mainly due to the difference in organic additives and ferrocene content between the two materials (Table 1). Indeed, the porous structure of these composites originates from the carbonaceous material decomposition (organic additives, phenolic resin, and ferrocene) [15]. The morphology of the KS44-20/CNT composite clearly shows stratified zones corresponding to the graphite particles of KS44 coated with amorphous carbon obtained upon the carbonization of the resin (Fig. 3(a)). Few CNTs grow vertically on the surface of the KS44-(20)/CNT carbon support (Fig. 3(a) and (b)). This reflects ferrocene's role as metal catalyst precursor reagent in synthetically useful and as a carbon source (cyclopentadienyl) upon its thermal decomposition to produce carbon nanotubes (CNTs). When focusing on areas inside the pores of KS44-(20)/CNT in Fig. 3(c) and Fig. 3(d), we observed large amounts of small CNTs growing, which are responsible for the hydrophobic character of the pores in the composite material.

Fig. 4 shows the Raman spectra of the synthesized graphite carbon and graphite carbon/CNT composites. Raman spectra exhibit typical D and G main bands located around 1,320 and 1,570 cm^{-1}, respectively [28]. The peak located around 2,700 cm^{-1} is attributed to the second-order 2D mode [29]. The sensitivity of the D-band to structural defects in the graphitic sp^2 network allows the Raman intensity ratio I_D/I_G between the D and G modes to be widely used to quantify the structural order degree of graphitic phases [28-31]. The percentage 'f' of disordered carbon can then be estimated ac-

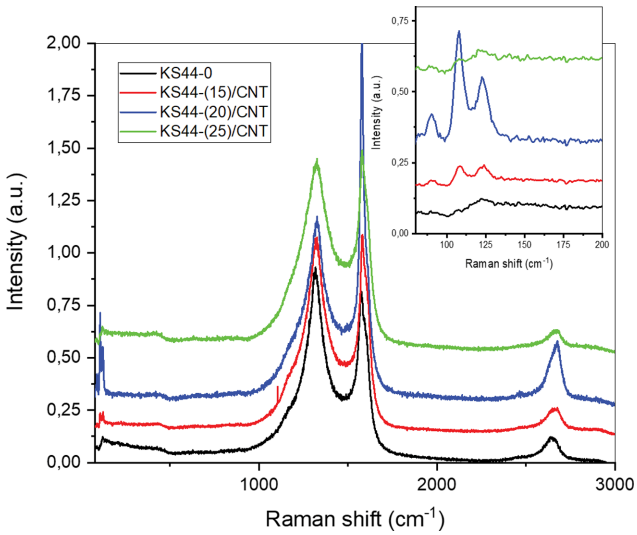

Fig. 4. Raman spectra of graphite carbon composites with and without CNT. Intensities are normalized on the signal of the D mode. The inset is a magnification of the low energy range.

Table 2. Values of Raman intensity ratio I_D/I_G, f (%) related to the amount of disordered carbon and electrical resistance of porous carbon composites

Composites	I_D/I_G	f (%)	R (Ω)
KS44-0	1.34	57.3	1.43 (0.15)
KS44-(15)/CNT	0.95	48.9	0.89 (0.13)
KS44-(20)/CNT	0.50	33.5	0.76 (0.12)
KS44-(25)/CNT	0.83	45.6	0.83 (0.09)

cording to Eq. (6) and the results are reported in Table 2.

$$f(\%) = \frac{I_D}{I_D + I_G} \times 100 \quad (6)$$

For the KS44-0 sample, the ratio (I_D/I_G) was 1.34, which is considered as a high value corresponding to the disordered carbon amount, estimated to be 57.3% of amorphous carbon [32]. We have already shown that the carbonization process of thermosetting phenolic resin gives rise to carbon composite that is mainly amorphous [15]. Otherwise, the percentage of disordered carbon stays lower than 50% in the samples obtained by ferrocene addition, with the lowest value of 33.5% observed for KS44-20/CNT. The increase of structural order in the composite graphite carbon/CNT materials agrees with the growth of more ordered phases, i.e., carbon nanotubes, whose presence is also attested by the appearance of weak and low energy Raman signals (presumably related to radial modes) around 110 and 125 cm^{-1} in the KS44/CNT and, more particularly, KS44-20/CNT [33]. The resonant Raman intensity of the RBM feature (e.g., radial breathing mode, (~100-300 cm^{-1})) corresponds to the coherent vibration of the C atoms of the carbon nanotubes (CNTs) in the radial direction, as if the tubes were breathing [33].

The electrical resistance decreases with the addition of ferrocene (Table 2), whose low value is 0.76 Ω in the presence of the KS44-20/CNT composite. In fact, the presence of CNTs, with a high conductivity, is at the origin of this evolution [34]. On the other hand, the high porosity observed as a function of the addition of ferrocene and in particular KS44-20/CNT does not justify this decrease. Such a decrease in resistance in the presence of the pores is well justified by a well interconnected porosity structure through the CNTs growing in the pores as shown on SEM observations.

2. Degradation of AO7 by the EF Process

2-1. Kinetics of Degradation

Fig. 5 depicts the effectiveness of graphite carbon/CNT electrodes in removing dye pollutants such as AO7. The degradation tests were carried out as a function of time in the absence (KS44-0 and KS44-x/CNT) and in the presence of the ferrous sulfate heptahydrate as a catalyst (KS44-0/Fe). This efficient AO7 degradation observed on the different electrodes with high porosity is quite stable under the experimental conditions adopted. Complete color removal of AO7 dye solution could be reached after 15 min, leading to the fast and highest AO7 decomposition at the early period of electrolysis originated from the breakage and destruction of Azo bonds of dye molecules [11,12]. The results clearly show that the presence of CNTs on the surface and inside the pores significantly upgrades the degradation of AO7. The efficiency of AO7 degradation by electro-Fenton process on the graphite carbon/CNT elec-

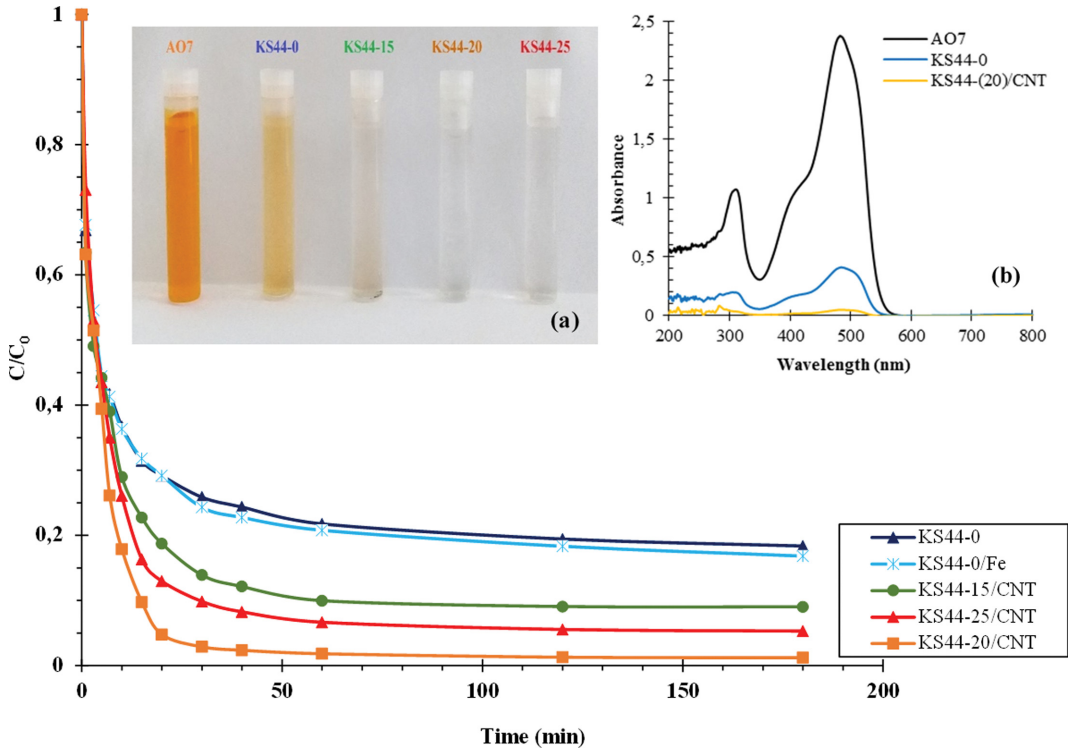

Fig. 5. Electro-Fenton degradation of AO7 dye (a) Evolution of the AO7 concentration with time during treatment with different electrodes (the inset reports images of the different AO7 solutions after treatment) and (b) absorption spectrum of initial AO7 and treated solutions after 2 h treatment.

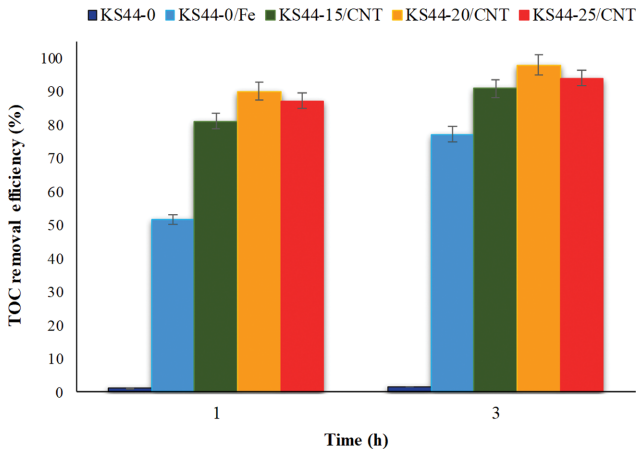

Fig. 6. TOC removal efficiency (%) of AO7 on porous carbon electrodes.

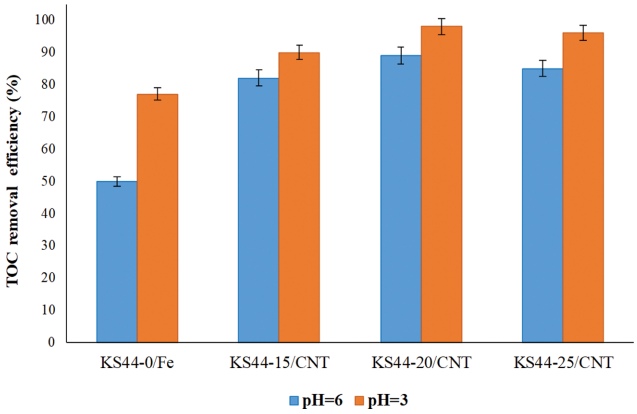

Fig. 7. Effect of pH medium in TOC removal efficiency (%) after 3 h on porous carbon electrodes.

trodes is ascribed to the performance improvement of electroactive surface and the conductivity enhanced by the presence of CNT, thus improving the electrochemical properties. The absorption band related to azo bond (wavelength at 484 nm) practically disappeared after 2 h of EF treatment with KS44-20/CNT (Fig. 5(b)).

2-2. Kinetics of Mineralization

As shown in Fig. 6, the mineralization rate increases from KS44-0 to KS44-20/CNT. In particular, the mineralization of AO7 in aqueous solution without $FeSO_4{\cdot}7H_2O$, as catalyst in the Fenton reagent, is rapidly obtained by using graphite carbon/CNT electrodes. The TOC removal efficiently reaches 90%, 96% and 98% after 3 hours of EF treatment with the KS44-(15)/CNT, KS44-(25)/CNT and KS44-(20)/CNT electrodes, respectively. However, only 2% TOC removal efficiency is observed after 3 h treatment with the KS44-0 electrode. In the presence of $FeSO_4{\cdot}7H_2O$, partial mineralization of 65% occurs with the KS44-0 electrode, together with relatively low kinetic degradation compared to the graphite carbon/CNT electrodes.

During the manufacturing process of the electrodes KS44-15/CNT, KS44-20/CNT and KS44-25/CNT, we used a percentage of ferrocene of 15, 20 and 25, respectively, as catalyst for the CNTs growth. After consolidation, the carbon structure of the electrodes presents iron particles [15]. The concomitant presence of iron playing the role of precursor to catalyze the EF process (for KS44-0/Fe), on the one hand, and the increasing amount (%) of ferrocene used for the different synthesized CNTs composites, on the other, explains the increase of the TOC removal efficiency of the graphite carbon/CNT composite electrodes compared to KS44-0. It is interesting to note that graphite carbon/CNT electrodes do not need ferrous sulfate heptahydrate catalyst in the AO7 solution for effective electro-Fenton process [35,36]. This shows how CNTs together with Fe play a more effective role as a heterogeneous catalyst than ferrous sulfate heptahydrate for EF process.

The pH value of the aqueous solution is also a key parameter for the EF process efficiency. Fig. 7 reveals the significant increase of the TOC removal when the pH is decreased from the initial value pH~6 to the adjusted pH=3, for all the electrodes under investigation. After 3 hours of electrolysis, almost total mineralization reached a TOC removal of 90%, 98%, and 96% on the KS44-15/CNT, KS44-20/CNT and KS44-25/CNT, respectively, yet stayed lower on the KS44-0 electrode with $FeSO_4{\cdot}7H_2O$, as catalyst (77%) [14,36]. As a result, pH adjustment (i.e., making it more acidic) plays a key role in maintaining stable performance of the electro-Fenton system, which accords well with the results found in literature reports [14,36].

In all experiments, the KS44-20 electrode (containing 20 wt% of ferrocene powder as catalyst for CNTs growth) was shown as the most optimal cathode due to its high mineralization efficiency towards the dye. The electrochemical activity as cathode leads to more than 98% of both AO7 color and TOC removals. When adding iron in solution ($FeSO_4{\cdot}7H_2O$), the iron hydroxide $Fe(OH)_3$ precipitates, especially at high pH values [37], with difficulty to be mineralized by hydroxyl radicals (HO') formed through EF process [39,40], which clearly explains the lower degradation efficiency when using homogeneous electro-Fenton (*i.e.*, addition of $FeSO_4$) (Fig. 8). The containment of iron particles in the carbon graphite/CNT electrodes will then eliminate the risk of any precipitates in the solution in the short- and long-term periods.

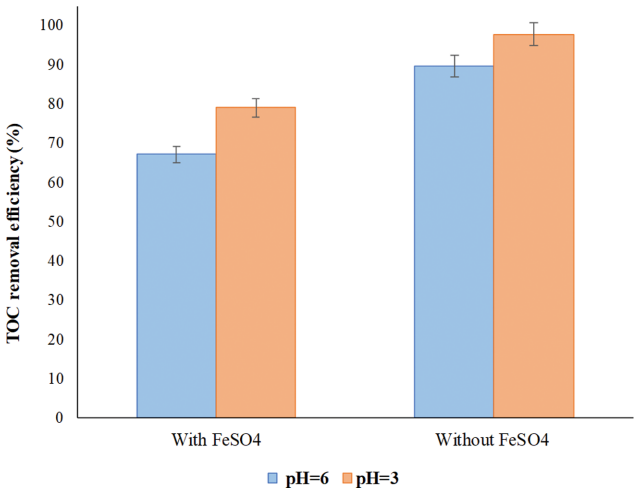

Fig. 8. Effect of $FeSO_4$ ($[Fe^{2+}]$) in TOC removal efficiency (%) after 3 h with KS44-(20)/CNT as cathode at pH=3 and pH=6.

Table 3. Degradation and mineralization efficiency of AO7 by EF process using different cathode materials. CF: Carbon felt; CPR-CF: Graphene-based modified carbon felt cathode; NPC/CF: Nitrogen-doped graphitized carbon cathode; CNTF/CF: Carbon nanotube fiber-based cathode; LDH/CF: Layered double hydroxide modified carbon felt cathode

Cathode material	Condition				Color removal (%)	Time (min)	TOC removal (%)	Time (hours)	Refs.
	Anode	I (mA/cm^2)	pH	[Fe^{2+}] (mM)					
CF	Pt	20	3	0.2	-	-	60	8	[11]
CPR-CF	Pt	20	3	0.2	-	-	94	8	[11]
CF	Pt	2.5	3	0.2	-	-	60	8	[12]
NPC/CF	Pt	2.5	3	0.2	97	30	90	8	[12]
CF	Ni/Ti	3.1	3	0.2	-	-	24	8	[13]
CNTF/CF	Ni/Ti	3.1	3	0.2	-	-	97	8	[13]
LDH/CF	Ti_4O_7	7.5	3	0.2	-	-	77	8	[14]
			6	0.2	-	-	69	8	
			9	0.2	-	-	58	8	
KS44-0	Pt	10	3	0.2	82	40	77	3	This work
				0	84	40	2	3	
			6	0.2	82	45	50	3	
				0	83	45	1	3	
KS44-15	Pt	10	3	0.2	-	30	-	3	
				0	89	30	90	3	
			6	0.2	-	30	-	3	
				0	88	30	82	3	
KS44-20	Pt	10	3	0.2	97	20	79	3	
				0	98	20	98	3	
			6	0.2	96	20	67	3	
				0	97	20	90	3	
KS44-25	Pt	10	3	0.2	-	25	-	3	
				0	95	25	96	3	
			6	0.2	-	25	-	3	
				0	94	25	85	3	

The results pertaining to the degradation and mineralization efficiencies obtained in this work are summarized in Table 3 and compared with those from other studies previously reported and using different cathode materials [11-14].

Le et al. [11] used a graphene modified cathode which effectively removed the color of AO7. On the other hand, the mineralization was almost complete (94.3%) in 8 h of EF treatment under an optimal applied current density (20 mA/cm^2). The cathode exhibited a greater mineralization efficiency (64%) in 2 h. In previous research works, the study of the adsorption capacity and that of the behavior of the NPC/CF material prepared by Le et al. [12] were proven as a cathode for the removal of AO7 by electro-Fenton process. When used as an adsorbent, NPC/CF demonstrated a great adsorption capacity with 97% color removal of AO7 (0.02 mM) after 30 min, reaching more than 90% of TOC removal within 8 h.

Another study [13] used a bio-refractory pollutant (AO7) to be treated by the CNTF/CF cathode in an acidic medium (pH=3). The results revealed that the azo dye (AO7) was completely mineralized by the EF process. In fact, 96.7% of the TOC was removed in 8 hours of electrolysis by applying a current density of 3.1 mA/cm^2 when the ferrous ions as catalyst (0.2 mM) was added into the AO7 solution. Meanwhile, only 23.7% of TOC removal was found on the raw CF support. Moreover, TOC removal yields of (77, 69 and 58%) in 8 h were obtained by the electro-Fenton studies of Ganiyu et al. [14], over a wide pH range at (pH=3, pH=6 and pH=9, respectively) using the LDH/CF cathode, by applying a current density of 7.5 mA/cm^2 when the ferrous sulfate heptahydrate as catalyst (0.2 mM) was added into the AO7 solution.

The results confirmed that graphite carbon/CNT electrodes materials are highly electrochemically active and behave differently in the EF process for the removal of AO7, under optimal conditions (pH=3 and I=20 mA and [Fe^{2+}]=0).

3. Adsorption of AO7 on Porous Carbon Composites

Fig. 9 reports the adsorption kinetics of AO7 on graphite electrodes as the evolution of $C(t)/C_0$ as a function of time (t), for different AO7 initial concentrations (C_0). The obtained results show that the adsorption efficiency decreases with the increase of the

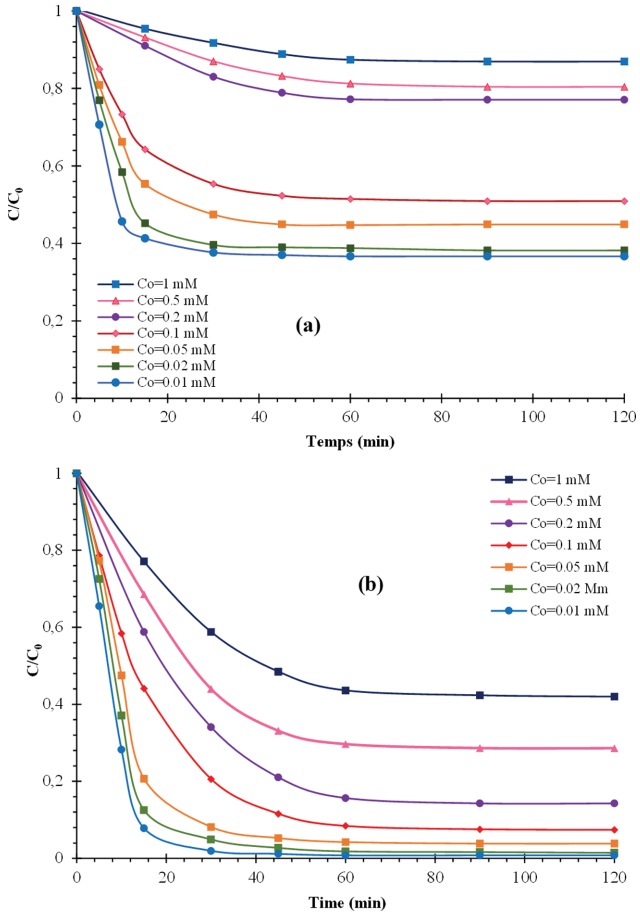

Fig. 9. Adsorption degradation of AO7 dye on porous carbon electrodes: (a) KS44-0 and (b) KS44-(20)/CNT.

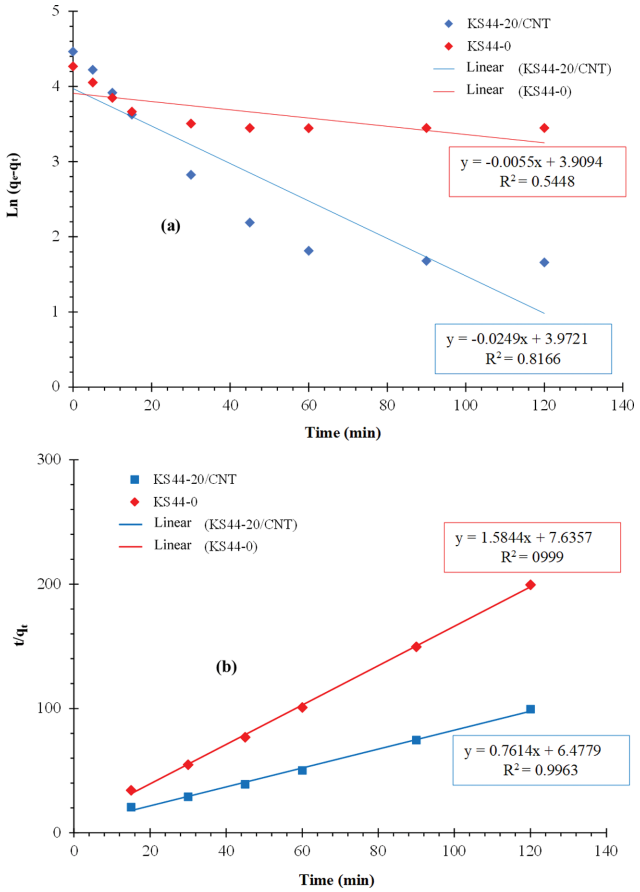

Fig. 10. Kinetic parameters of the pseudo-first-order model (a) and the pseudo-second-order model (b) for AO7 adsorption on KS44-0 and KS44-20/CNT.

initial AO7 concentration. At the lower initial concentration (0.01 mM), the adsorption efficiency of AO7 after 60 min is 100% and 63% for KS44-20/CNT and KS44-0, respectively. At [AO7]=0.1 mM, the adsorption reaches equilibrium after 40 min for KS44-0, with 47% efficiency, and 1 h for KS44-20/CNT, with 91% efficiency. Indeed, the enhanced AO7 adsorption capacity and efficacy observed with KS44-20/CNT is related to the presence of carbon nanotubes that severely grew within the material, giving rise to pores and, thus, higher specific surface area (Table 2). Nevertheless, the adsorption activity decreases with the increase in AO7 dye initial concentration because of the saturation of the adsorption active sites both on the internal and external surface of the carbon composites. While equilibrium adsorption isotherms are important to confirm this idea, studying the adsorption isotherm reflects the equilibrium distribution of the adsorbate (the solute AO7) between the bulk phase, where the volume concentration is C_e (mol·L^{-1}), and the adsorbent solid surface of carbon electrodes, where the surface concentration is q_e (mg·g^{-1}) [41-44]. Langmuir and Freundlich equations [45-49] were applied to quantify the adsorption capacity of KS44-0 and KS44-20/CNT for AO7.

The adsorption kinetics of AO7 (C_0=0.1 mM) by graphite composites electrodes KS44-0 and KS44-20/CNT was evaluated to describe the controlling mechanism of the adsorption process according to the pseudo-first order and pseudo-second order model equations.

The pseudo-first-order kinetic model, considering the impact of the initial AO7 concentration on the adsorption process, can be expressed as [42,43]:

$$\frac{1}{q_t}=\frac{k_1}{q_1\times t}+\frac{1}{q_1} \tag{7}$$

where q_t (mg·g^{-1}) is the adsorbed amount of AO7 at time t, q_1 (mg·g^{-1}) is the maximum adsorption capacity and k_1 (min^{-1}) is the adsorption rate constant. According to this model, a pseudo-first order constant can be determined by extrapolation of the plot $\ln(q_e-q_t)$ vs (time) (Fig. 10(a)) according to the following pseudo-first-order kinetic equation [42,43]:

$$\ln(q_e-q_t)=\ln(q_e)-\frac{k_1}{2.303}\times t \tag{8}$$

It is clear that the pseudo-first-order kinetic equation does not fit the experimental values as observed in Fig. 10(a) and regarding the correlation coefficients in Table 4.

The pseudo-second-order kinetic model was then applied to assess the process of the AO7 absorbed surface concentration over time. According to [42,43], the linear form of the pseudo-second-order kinetic equation can be expressed as:

Table 4. Kinetic parameters for AO7 adsorption (C_0=0.1 mM) on KS44-0 and KS44-20

	KS44-0	KS44-20
Pseudo-first-order		
k_1 (min^{-1})	0.005	0.024
q_1 ($mg{\cdot}g^{-1}$)	49.869	53.095
R_1^2	0.5448	0.8166
Pseudo-second-order		
k_2 ($g{\cdot}mg^{-1}{\cdot}min^{-1}$)	1.677	0.285
q_2 ($mg{\cdot}g^{-1}$)	0.606	1.226
R_2^2	0.999	0.9963

$$\frac{t}{q_t}=\frac{1}{(k_2\times q_e^2)}+\frac{t}{q_e} \quad (9)$$

where q_e ($mg{\cdot}g^{-1}$) is the maximum adsorption capacity and k_2 ($g{\cdot}mg^{-1}{\cdot}min^{-1}$) is the rate constant of adsorption. Pseudo-order constants have been determined by the extrapolation of the plot (t/q_t) vs (time) (Fig. 10(b)). The calculated k_1, k_2, q_1, q_2 and correlation coefficients R_1^2 and R_2^2 and are reported in Table 4.

Fig. 10 and Table 4 show that the correlation coefficients for the pseudo-second order kinetic model (R_1^2=0.999 and 0.9963) are higher than for the pseudo-first-order kinetic model (R_2^2=0.5449 and 0.8116). The obtained results attest that the adsorption fits better with the pseudo-second-order kinetic model [44].

3-1. Adsorption Isotherm Models

The adsorption isotherms of AO7 on the KS44 composites at room temperature were studied (Fig. 11 and Fig. 12). Actually, the adsorption isotherm describes the interaction of dyes with adsorbent, which is a determining factor for the performance of adsorption processes. Many models have been applied to analyze experimental sorption equilibrium data [45-48]. The Langmuir isotherm model is effective for monolayer reversible adsorption on a homogeneous surface (all adsorption sites are identical) and can be applied

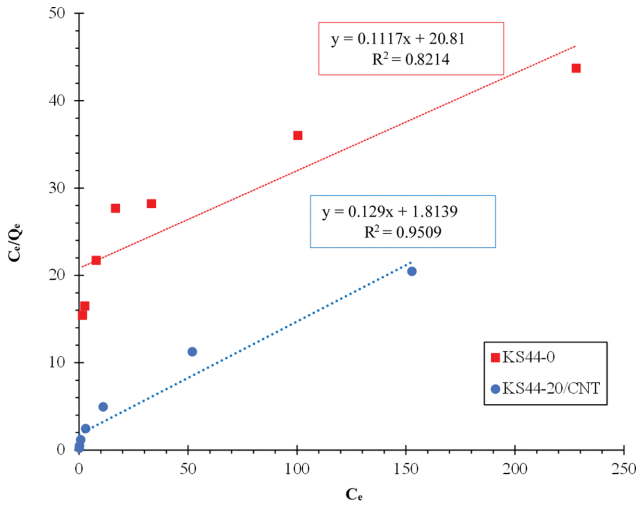

Fig. 11. Langmuir adsorption isotherms of porous carbon composites.

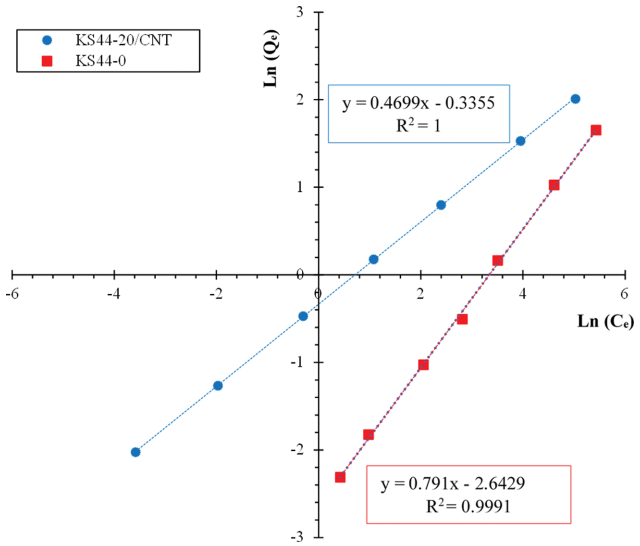

Fig. 12. Freundlich adsorption isotherms of porous carbon composites.

to predict the maximum monolayer adsorption capacity of the adsorbent at surface saturation [46,47]. The equation can be expressed as [48]:

$$q_e=\frac{q_{max}\times K_L\times C_e}{1+K_L\times C_e} \quad (10)$$

where K_L ($L{\cdot}mg^{-1}$) is the Langmuir adsorption equilibrium constant, which is characteristic of the interaction between the active surface site and the adsorbate (AO7) and q_{max} ($mg{\cdot}g^{-1}$) is the maximum adsorption retained by the adsorbent at surface saturation [48]. A linear form of the Langmuir equation can be obtained by taking logarithms of the equation:

$$\frac{C_e}{q_e}=\frac{C_e}{q_{max}}+\frac{C_e}{(q_{max}\times K_L)} \quad (11)$$

The Freundlich isotherm model is an empirical equation that assumes multilayer adsorption on heterogeneous adsorption sites, and the adsorption capacity is influenced by the adsorbate equilibrium concentration [49,50]. The equation can be expressed as [48]:

$$q_e=K_F\times C_e^{1/n} \quad (12)$$

where K_F and 1/n represent the Freundlich characteristic constants. K_F represents the adsorption capacity and 1/n the adsorption intensity. A linear form of the Freundlich equation can be obtained by taking logarithms of the equation:

$$\ln(q_e)=\left(\frac{1}{n}\right)\times\ln(C_e)+\ln(K_F) \quad (13)$$

Table 5 presents the values of the Langmuir and Freundlich constants, extrapolated from the equations of both models (Fig. 11 and Fig. 12). The correlation coefficient (R^2) of the linear representations of the Freundlich equation is higher than that of the Langmuir equation for both samples. Thus, the values of the Freundlich constant (n=1.264 and n=2.1281), i.e., n>1, dictate a favorable adsorption of AO7 on the KS44-0 and KS44-20 composites, respec-

Table 5. Constants of the adsorption kinetics: Langmuir and Freundlich isotherms

Electrodes	Langmuir-Isotherm			Freundlich-Isotherm		
	q_{max} (mg·g^{-1})	K_L (L·mg^{-1})	R^2	K_F (mg·g^{-1})	N	R^2
KS44-0	8.952	186.302	0.9942	0.071	1.264	0.9991
KS44-20	7.751	14.061	0.9509	0.714	2.128	1

tively [51]. These results show that the AO7 adsorption behavior on KS44-0 and KS44-20 better fits with the Freundlich model, indicating the absorption of AO7 as a multilayer mechanism [52-55]. The K_F value is higher for KS44-20 than for KS44-0, which confirms a more important adsorption capacity for KS44-20 as observed in Fig. 9 and Table 4.

4. System Coupling Adsorption and Electro-Fenton Degradation

Moreover, the adsorption experiments were performed after the immersion of the carbon cathode in the aqueous solution of AO7 (0.1 mM initial concentration), with no current source and no bubbling oxygen. As a result, the retention of AO7 dye by adsorption method attained more than 84% in 120 min for the KS44-(20)/CNT cathode, compared to 42% during 120 min for the KS44-0 cathode (Fig. 13). Once adsorption equilibrium was reached (after 2 hours), the electric current was turned on at 20 mA and the oxygen flowed through the system to start the EF process. The EF experiments were carried out after the adsorption step of the dye. The azo dye pollutant (AO7) was then totally removed in 5 and 45 min by KS44-(20)/CNT or KS44-0 cathodes, respectively. These results clearly proved a long-term stability and system durability due to the continuous regeneration of the KS44-(20) cathode after 5 cycles of use, which allowed processing efficiency and reusability without any decrease of the catalytic activity in time. The •OH radical attack started the process, resulting in the formation of two hydroxylated AO7 molecules. However, researchers [35] have reported the formation of those intermediates during the photocatalytic degradation of azo dye in aqueous solution. These hydroxylated intermediates were oxidized to produce naphthalene-like compounds that could be identified. The azo bond was then attacked by the •OH radical, giving birth to naphthalene-type products. The latter were decomposed into aromatic by-products by continuous •OH radical action. Short-chain carboxylic acids were produced by degrading these aromatic by-products. These organic acids were finally broken down into CO_2, H_2O, and inorganic ions.

Additionally, the Langmuir kinetics type was investigated to study the degradation process of organic dye (AO7).

The apparent first-order rate constants (k_{app}) were obtained by plotting the Ln([AO7]/[AO7]$_0$) against time [56] (Fig. 14), using the equation [57]:

$$\ln\frac{C}{C_0} = -k_{app}t \tag{14}$$

where (C_0) is the initial dye concentration (mg/L), (C) the equilibrium dye concentration (mg/L), (k_{app}) the apparent constant (min^{-1}) and (t) the electrolysis time (min). Thus, the values of apparent constants (k_{app}) are 0.17 and 0.12 min^{-1} for KS44-(20)/CNT and KS44-0 cathodes with R^2=0.998 and 0.997, respectively, revealing

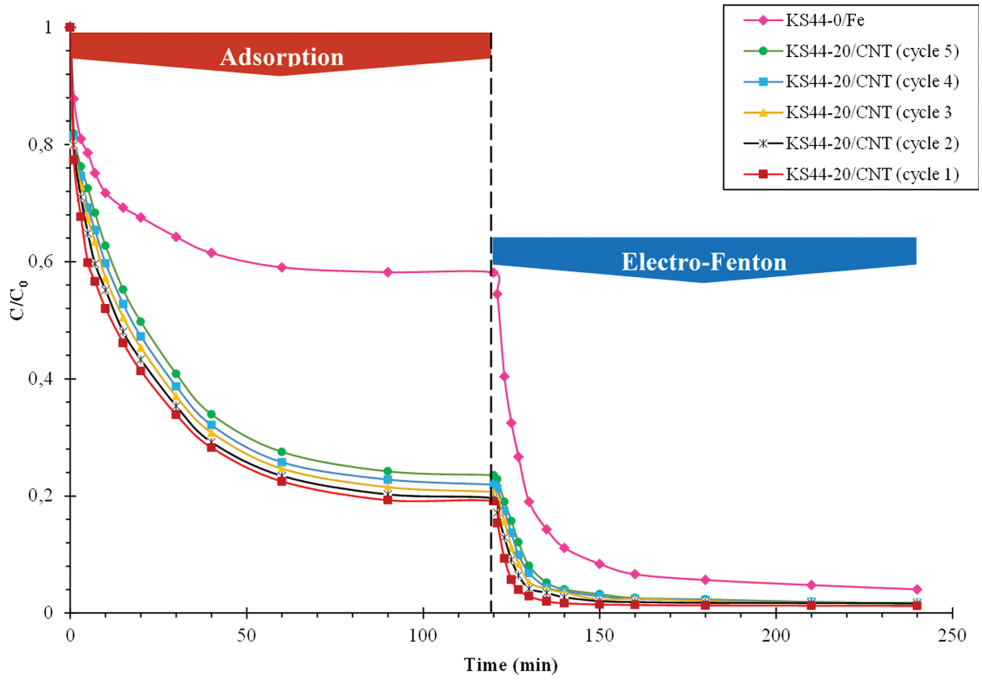

Fig. 13. Kinetics of AO7 removal by both adsorption and electro-Fenton processes on KS44-0/Fe and KS44-20/CNT electrodes.

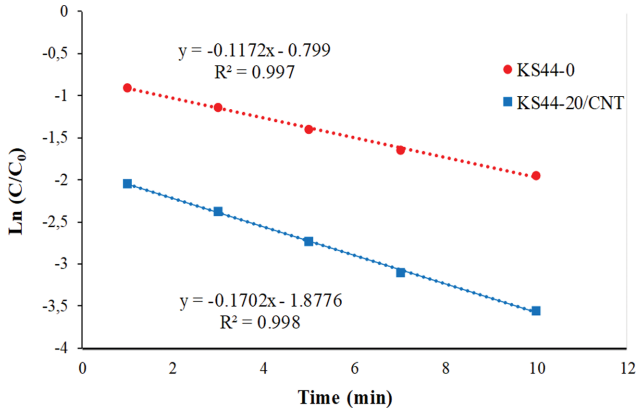

Fig. 14. The plot of Ln([AO7]/[AO7]$_0$) versus time for each carbon electrodes: (a) KS44-0 and (b) KS44-(20)/CNT.

the importance of modifying the carbon based membranes with CNTs for coupling adsorption and EF process.

CONCLUSION

Carbon electrodes were investigated with the aim of improving the performance of combining the adsorption and EF processes for full mineralization and destruction of azo dyes in wastewater. Electrodes exhibited were used as multifunctional materials acting both as adsorbent and active cathode in the EF process for the removal and destruction of AO7 dye as a model of persistent water pollutants. It is particularly interesting that the presence of CNTs within the carbon electrodes (containing 20 wt% of ferrocene as catalyst for CNTs growth) can maximize the degradation and mineralization efficiency of AO7 during the EF process. The presence of iron particles as precursors on the graphite carbon/CNT electrodes allowed us to improve the mineralization rate of AO7 by EF process compared to the graphite carbon electrode developed without ferrocene compound. Furthermore, the degradation and mineralization of AO7 dye with the initial concentration of 0.1 mM were almost complete (98% color and TOC removals) after only 3 h of electrolysis time. The apparent rate constant for the KS44-(20)/CNT and KS44-0 electrodes was 0.17 and 0.12 min^{-1}, respectively. It has been demonstrated that graphite carbon/CNT electrodes exhibited high electrochemical performance, long-term stability and system durability due to continuously operating treatment, allowing their reusability without any decrease of the catalytic activity in time after five cycles of use.

ABBREVIATIONS

CNTs : carbon nanotubes
AO7 : acid orange 7
AOPs : advanced oxidation processes
EF : electro-Fenton process
TOC : total organic carbon
SEM : scanning electron microscope
BET : Brunauer-Emmett-Teller theory
I_D : intensity of D band
I_G : intensity of G band
f (%) : amount of disordered carbon
R : electrical resistance
I : current
pH : potential of hydrogen
Pt : platinum
Na_2SO_4 : anhydrous sodium sulfate
$FeSO_4{\cdot}7H_2O$: iron (II) sulfate heptahydrate
$Fe(OH)_3$: iron hydroxide
H_2SO_4 : sulfuric acid
$Fe(C_5H_5)_2$: ferrocene powder
Fe^{2+} : ferrous ion
Fe^{3+} : ferric ion
H_2O_2 : hydrogen peroxide
O_2 : molecular oxygen
OH^- : hydroxide
H^+ : hydrogen ion
•OH : hydroxyl radical
C_0 : initial dye concentration
C_e : equilibrium dye concentration
q_t : adsorbed amount of AO7 at time t
q_1 : maximum adsorption capacity for the pseudo-first-order adsorption
k_1 : adsorption rate constant for the pseudo first-order-adsorption
q_e : maximum adsorption capacity
k_2 : rate constant of adsorption for the pseudo-second-order adsorption
R^2 : correlation coefficient
k_{app} : apparent constant
t : electrolysis time
K_L : Langmuir adsorption equilibrium constant
q_{max} : maximum adsorption
K_F and 1/n : Freundlich characteristic constants

NOMENCLATURE

KS44 : pure graphite carbon powder
KS44-0 : graphite carbon composite (developed without carbon nanotubes)
KS44/CNT : graphite carbon/carbon nanotubes composites
KS44-15/CNT : graphite carbon/carbon nanotubes composite (containing 15 wt% of ferrocene)
KS44-20/CNT : graphite carbon/carbon nanotubes composite (containing 20 wt% of ferrocene)
KS44-25/CNT : graphite carbon/carbon nanotubes composite (containing 25 wt% of ferrocene)

SUPPORTING INFORMATION

Additional information as noted in the text. This information is available via the Internet at http://www.springer.com/chemistry/journal/11814.

REFERENCES

1. A. E. D. Mahmoud, M. Fawzy and M. M. A. Abdel-Fatah, Techni-

cal Aspects of Nanofiltration for Dyes Wastewater Treatment, Membrane Based Methods for Dye Containing Wastewater, Springer, Singapore, 23-35 (2022).
2. A. E. D. Mahmoud and M. Fawzy, Nanosensors and Nanobiosensors for Monitoring the Environmental Pollutants, Waste Recycling Technologies for Nanomaterials Manufacturing, 229-246 (2021).
3. E. Brillas, I. Sires and M. A. Oturan, *Chem. Rev.*, **109**, 6570 (2009).
4. M. A. Rodrigo, N. Oturan and M. A. Oturan, *Chem. Rev.*, **114**, 8720 (2014).
5. S. Ayedi, I. Jedidi, M. Rivallin, F. Gillot, S. Lacour, S. Cerneaux, M. Cretin and R. Ben Amar, *J. Membr. Sci.*, **466**, 42 (2013).
6. M. A. Oturan and J. J. Aaron, *Crit. Rev. Environ. Sci. Technol.*, **44**, 2577 (2014).
7. K. W. Jung, D. S. Park, M. J. Hwang and K. H. Ahn, *Ultrason. Sonochem.*, **26**, 22 (2015).
8. C. Trellu, B. P. Chaplin, C. Coetsier, R. Esmilaire, S. Cerneaux, C. Causserand and M. Cretin, *Chemosphere*, **208**, 159 (2018).
9. M. Diagne, N. Oturan and M. A. Oturan, *Chemosphere*, **66**, 841 (2007).
10. A. Ozcan, M. A. Oturan, N. Oturan and Y. Sahin, *J. Hazard. Mater.*, **163**, 1213 (2009).
11. T. X. H. Le, M. Bechelany, S. Lacour, N. Oturan, M. A. Oturan and M. Cretin, *Carbon*, **94**, 1003 (2015).
12. T. X. H. Le, R. Esmilaire, M. Drobek, M. Bechelany, C. Vallicari, S. Cerneaux, A. Julbe and M. Cretin, *J. Phys. Chem. C*, **121**, 15188 (2017).
13. T. X. H. Le, B. Alemán, J. J. Vilatela, M. Bechelany and M. Cretin, *Front. in Mater.*, **5**, 1 (2018).
14. S. O. Ganiyu, T. X. H. Le, M. Bechelany, N. Oturan, S. Papirio, G. Esposito, E. D. van Hullebusch, M. Cretin and M. A. Oturan, *Chem. Eng. J.*, **350**, 844 (2018).
15. S. Zghal, I. Jedidi, M. Cretin, S. Cerneaux and M. Abdelmouleh, *Diam. Relat. Mater.*, **101**, 107557 (2020).
16. S. K. Khare, K. K. Ponday, R. M. Srivastrara and V. N. Singh, *Env. Tech. Let.*, **9**, 1163 (1988).
17. IARC (International Agency for research on cancer), Monographs on the evaluation of the carcinogenic risk of chemicals to humans, **29**, Lyon, France (1982).
18. H. Ben Mansour, O. Boughzala, D. Dridi, D. Barillier, L. Chekir-Ghedira and R. Mosrati, *J. Water Sci.*, **24**, 209 (2011).
19. C. Mills, R. J. Bull and K. P. Cantor, *Maladie Chronique au Canada*, **19**, 3 (1998).
20. H. Lin, Removal of organic pollutants from water by indirect electro-oxidation using hydroxyl and sulphate radical species, Elimination des pollutants organiques de l'eau par electrochimie indirect basee sur les radicaux hydroxyls and sulphates, *HAL* 1-164 (2006).
21. I. Arslan, I. A. Balcioglu and D. W. Bahnemann, *Appl. Catal. B-Environ.*, **26**, 193 (2000).
22. T. Tasaki, T. Wada, K. Fujimoto, S. Kai, K. Ohe, T. Oshima, Y. Baba and M. Kukizaki, *J. Hazard. Mater.*, **162**, 1103 (2009).
23. H. Y. Shu and M. C. Chang, *Dyes Pigm.*, **65**, 25 (2005).
24. M. Khadhraoui, H. Trabelsi, M. Ksibi, S. Bouguerra and B. Elleuch, *J. Hazard. Mater.*, **161**, 974 (2009).
25. A. E. D. Mahmoud, K. M. Al-Qahtani, S. O. Alflaij, S. F. Al-Qahtani and F. A. Alsamhan, *Sci. Rep.*, **11**, 1 (2021).
26. B. Chen, G. Zhong, P. Goldberg Oppenheimer, C. Zhang, H. Tornatzky, S. Esconjauregui, S. Hofmann and J. Robertson, *ACS Appl. Mater. Interfaces*, **7**, 3626 (2015).
27. K. S. Sing, *Pure Appl. Chem.*, **57**, 603 (1985).
28. Y. Wang, D. C. Alsmeyer and R. L. Mc Creery, *Chem. Mater.*, **2**, 557 (1990).
29. A. C. Ferrari, *J. Solid State Commun.*, **143**, 47 (2007).
30. A. C. Ferrari and J. Robertson, *Phys. Rev. B*, **61**, 14095 (2000).
31. F. Tuinstra and J. L. Koenig, *J. Chem. Phys.*, **53**, 1126 (1970).
32. T. H. Ko, W. S. Kuo and Y. H. Chang, *Polym. Compos.*, **21**, 745 (2000).
33. Y. Park, K. P. S. S. Hembram, R. Yoo, B. Jang, W. Lee, S.-G. Lee, J.-G. Kim, Y.-I. Kim, D. J. Moon, J.-K. Lee and J.-K. Lee, *J. Phys. Chem. C*, **123**, 14003 (2019).
34. M. E. Mendoza, A. P. Campos, Y. Xing, D. C. Bell and I. G. Solórzano, *Diam. Relat. Mater.*, **110**, 108083 (2020).
35. T. X. H. Le, T. V. Nguyen, Z. A. Yacouba, L. Zoungrana, F. Avril, E. Petit, J. Mendret, V. Bonniol, M. Bechelany, S. Lacour, G. Lesage and M. Cretin, *Chemosphere*, **161**, 308 (2016).
36. Y. H. Guan, J. Ma, X. C. Li, J. Y. Fang and L. W. Chen, *Environ. Sci. Technol.*, **45**, 9308 (2011).
37. M. Hove, R. P. Hille and A. Lewis, *Chem. Eng. Sci.*, **63**, 1626 (2008).
38. H. Olvera-Vargas, J. C. Rouch, C. Coetsier, M. Cretin and C. Causserand, *Sep. Purif. Technol.*, **203**, 143 (2018).
39. C. Trellu, C. Coetsier, J. C. Rouch, R. Esmilaire, M. Rivallin, M. Cretin and C. Causserand, *Water Res.*, **131**, 310 (2018).
40. S. O. Ganiyu, N. Oturan, S. Raffy, M. Cretin, C. Causserand and M. A. Oturan, *Sep. Purif. Technol.*, **208**, 142 (2019).
41. A. E. D. Mahmoud, M. Franke, M. Stelter and P. Braeutigam, *Powder Technol.*, **366**, 629 (2020).
42. S. V. Mohan, N. C. Rao and J. Karthikeyan, *J. Hazard. Mater.*, **90**, 189 (2002).
43. S. V. Mohan, N. C. Rao, K. K. Prasad and J. Karthikeyan, *J. Waste Manag.*, **22**, 575 (2002).
44. H. Tang, W. Zhou and L. Zhang, *J. Hazard. Mater.*, **209**, 218 (2012).
45. A. E. D. Mahmoud, *J. Environ. Manage.*, **270**, 110911 (2020).
46. K. N. Aboua, D. B. Soro, M. Diarra, K. Dibi, K. R. N'Guettia and K. S. Traore, *Afr. Sci.*, **14**, 322 (2018).
47. A. E. D. Mahmoud, A. Stolle and M. Stelter, *ACS Sustain. Chem. Eng.*, **6**, 6358 (2018).
48. K. Y. Foo and B. H. Hameed, *Chem. Eng. J.*, **156**, 2 (2010).
49. A. Mittal, A. Malviya, D. Kaur, J. Mittal and L. Kurup, *J. Hazard. Mater.*, **148**, 229 (2007).
50. N. Unlu and M. Ersoz, *J. Hazard. Mater.*, **136**, 272 (2006).
51. A. Mittal, A. Malviya, D. Kaur, J. Mittal and L. Kurup, *J. Hazard. Mater.*, **148**, 229 (2007).
52. D. Mall, V. Srivastava and N. Agarwal, *Dyes Pigm.*, **690**, 210 (2006).
53. W. H. Cheung, Y. S. Szeto and G. MgKay, *Bioresour. Technol.*, **98**, 2897 (2007).
54. K. D. Belaid et S. Kacha, *J. Water Sci.*, **24**, 131 (2011).
55. M. S. Mohy Eldin, E. A. Soliman, A. A. Elzatahry, M. R. Elaassar, B. Y. Eweida, M. F. Elkady, A. M. Abdel Rahmand and M. Elsayed Yossef, *Desalin. Water Treat.*, **168**, 308 (2019).
56. M. Diagne, N. Oturan and M. A. Oturan, *Chemosphere*, **66**, 841 (2007).
57. M. Ismail, M. I. Khan, S. B. Khan, K. Akhtar, M. A. Khan and A. M. Asiri, *J. Mol. Liq.*, **268**, 87 (2018).

Supporting Information

Electroactive adsorbent composites of porous graphite carbon/carbon nanotube for highly efficient organic dye removal

Sabrine Zghal*, Ilyes Jedidi,†, Marc Cretin***,†, Sophie Cerneaux***, Didier Cot***, Serge Lagerge***, Stefano Deabate***, and Makki Abdelmouleh*,†**

*Laboratory of Materials Science and Environment (LMSE), Faculty of Science of Sfax (University of Sfax), Rte. Soukra Km 4, 3000 Sfax, Tunisia
**University of Technology and Applied Science - Sohar, Engineering Department, Al-Jamiaa street, P.O. Box, 135, Sohar, 311, OMAN
***Institut Européen des Membranes, IEM - UMR 5635, ENSCM, CNRS, Univ Montpellier, Montpellier, France
(*Received 6 November 2021 • Revised 2 March 2022 • Accepted 17 March 2022*)

Table S1. Paste formulation of porous carbon composites

Raw composites	Weight percent (wt%)			
	KS44-0	KS44-(15)/CNT	KS44-(20)/CNT	KS44-(25)/CNT
Phenolic resin	18	15.3	14.4	13.5
Ethanol	18	15.3	14.4	13.5
Carbon graphite	46	39.1	36.8	34.5
Avicel®	11	9.3	8.8	8.25
Ethylene glycol	7	6	5.6	5.25
Ferrocene	0	15	20	25

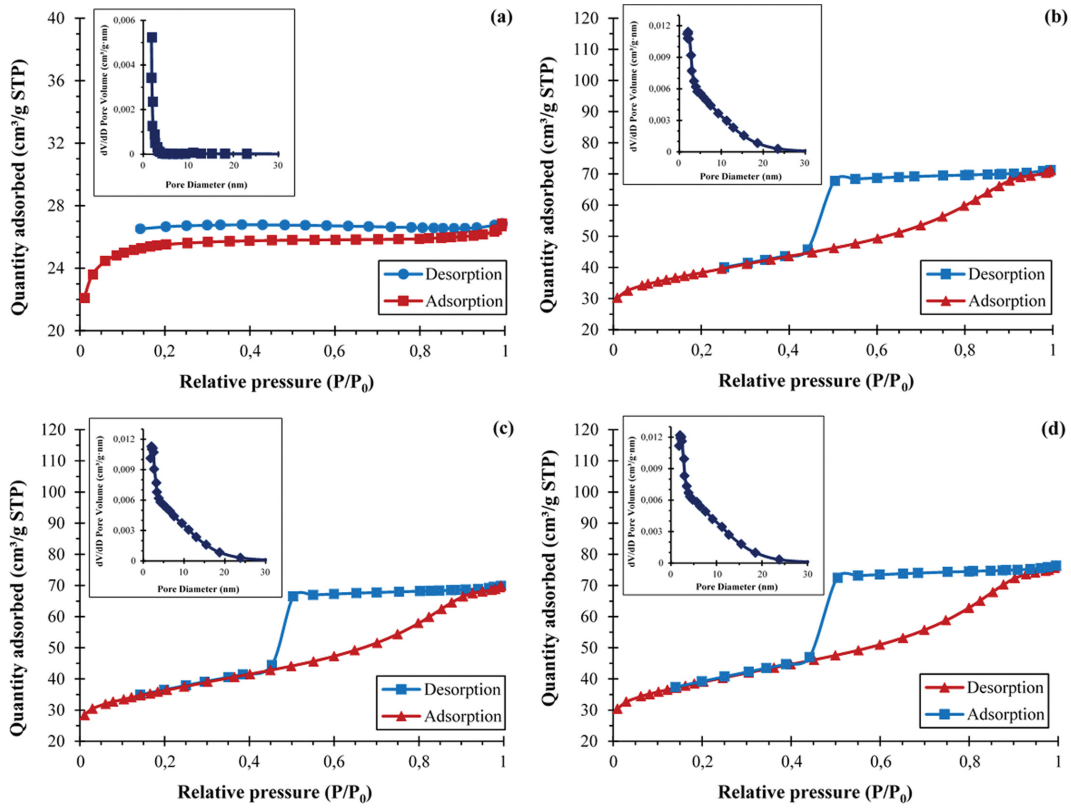

Fig. S1. Nitrogen adsorption-desorption isotherms and the pore size distributions of the carbon composites: (a) KS44-0, (b) KS44-15, (c) KS44-20 and (d) KS44-25.